Electrochemical CO Reduction: A Property of the Electrochemical Interface

Alexander Bagger,[†] Logi Arnarson,[†] Martin H. Hansen,[‡] Eckhard Spohr,[¶] and Jan Rossmeisl*[,†]

[†]Department of Chemistry, University of Copenhagen, Universitetsparken 5, 2100 Copenhagen, Denmark

[‡]SUNCAT Center for Interface Science and Catalysis, SLAC National Accelerator Laboratory, Menlo Park, California 94025, United States

[¶]Faculty for Chemistry and Center for Computational Sciences and Simulation, University of Duisburg-Essen, Universitätsstraße 2, D-45141 Essen, Germany

ABSTRACT: Electrochemical CO reduction holds the promise to be a cornerstone for sustainable production of fuels and chemicals. However, the underlying understanding of the carbon−carbon coupling toward multiple-carbon products is not complete. Here we present thermodynamically realistic structures of the electrochemical interfaces, determined by explicit ab initio simulations. We investigate how key CO reduction reaction intermediates are stabilized in different electrolytes and at different pH values. We find that the catalytic trends previously observed experimentally can be explained by the interplay between the metal surface and the electrolyte. For the Cu(100) facet with a phosphate buffer electrolyte, the energy efficiency is found to be limited by blocking of a phosphate anion, while in alkali hydroxide solutions (MOH, M = Na, K, Cs), OH* intermediates may be present, and at high overpotential the H* coverage limits the reaction. The results provide insight into the electrochemical interface structure, revealing the limitations for multiple-carbon products, and offer a direct comparison to experiments.

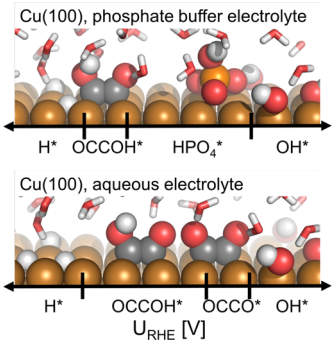

INTRODUCTION

Selective electrocatalytic reductions of carbon dioxide (CO_2) and carbon monooxide (CO) to sustainable fuels and chemicals by the use of renewable electricity and carbon sources are the dream reactions to complete the carbon cycle of modern society.[1,2] Advances have been made in the simplest two-electron reductions of CO_2 to CO[3−5] or formic acid.[6] However, the CO_2 reduction process still suffers from poor energy efficiency and selectivity.[7]

The further reduction of CO to single-carbon products[8] (CH_yO_z) and to multiple-carbon products ($C_xH_yO_z$), namely carbon−carbon coupling, or CC coupling,[9,10] has recently attracted attention with reports of experiments utilizing oxidized copper precursors.[11−13] Although the oxidized copper precursor catalyst shows high performance, a better understanding of the CC coupling mechanism is needed to give direction for better CC coupling selectivity and energy efficiency. The proposed mechanisms to distinguish single-carbon products and multiple-carbon products can be written as

$$CO(g) + * \rightarrow CO^* \rightarrow \text{protonation} \rightarrow \ldots \rightarrow CH_yO_z + *$$

$$2CO(g) + * \rightarrow 2CO^* \rightarrow OCCO^* \rightarrow \text{protonation} \rightarrow \ldots \rightarrow C_xH_yO_z + *$$

Single-facet studies[14−16] have shown that the Cu(100) facet has a unique capability to reduce CO to C_2H_4 at potentials lower than that at which the evolution of H_2 occurs. However, understanding the properties and limitations of the Cu catalyst, in particular of the Cu(100) facet, is key for improving the electrocatalytic CO conversion toward high-value products. We set out to answer the following questions regarding CO reduction to high-value products: Why is C_2H_4 evolution observed prior to H_2 evolution on Cu(100) and not on the other Cu facets? Why does the C_2H_4 evolution depend on the electrolyte and on pH? How does the C_2H_4 evolution depend on cations?

In order to answer these questions and find the underlying properties needed to produce multiple-carbon products from CO reduction, we study the reaction intermediates on the Cu(111), Cu(100), and Cu(110) facets by Ab Initio Molecular Dynamics (AIMD)[17,18] simulations of explicit electrolytes in contact with the surfaces.[19,20] The presence of electrolytes shows how differences in water behavior at the different electrode facets stabilize or destabilize the OCCO* and CO* intermediates. The interpretations of the results of the facets and of water solvation effects are in line with the trends revealed in our previous studies.[21]

The most interesting Cu(100) facet interface is treated by the Generalized Computational Hydrogen Electrode (GCHE),[22,23] ensuring that the structure of the interface is in equilibrium with the chemical potential for electrons, protons, and ions as determined by the electrochemical environment. This scheme

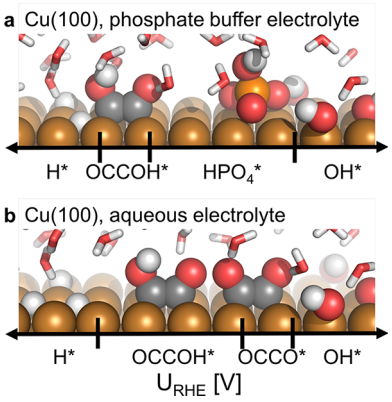

Figure 1. Combined snapshots of the AIMD simulation of the CC coupling electrochemical interface on Cu(100) for (a) the phosphate buffer at pH = 7 and (b) the aqueous electrolyte at pH = 13. Both figures show intermediate species coverage on a reversible hydrogen electrode potential scale. We note that the OCCO* dimer, OCCOH*, and H* are reaction intermediates, and hence the coverage of these is, in reality, determined by reaction rates and not equilibrium. In these simulations the reaction rate is assumed small, which means that the equilibrium assumption is valid.

allows us to explicitly calculate interface phase diagrams which include the structure of the electrolyte and pH.

This is the first study with realistic structures of the interface in equilibrium with the conditions, and we use these structures to explain experimental findings in terms of the reaction dependence on electrolyte and pH. These key finding are summarized in Figure 1, which schematically shows how a HPO_4^* anion blocks the surface at lower overpotential for the phosphate buffer and OH* intermediates may be present in the aqueous electrolyte, while at high overpotential CC coupling is limited by adsorbed hydrogen (H*).

RESULTS

CO* and OCCO* on Cu(111), Cu(100), and Cu(110). In order to understand the unique properties of the Cu metal catalyst to catalyze CO into multiple products electrochemically,[24−26] we investigate the Cu facets in terms of the binding energies of CO* and H*. This approach allows for classifying the different Cu facets according to their reactivity[21] and hereby answers the first question of why C_2H_4 is evolved prior to H_2 on Cu(100) and not on the other Cu facets.

In Figure 2a, the CO* and H* binding energies are found with BEEF-vdW[27,28] vacuum calculations (i.e., not including the electrolyte) and used to estimate the errors associated with the choice of functional. For Cu(100) and Cu(110) this has been done with respect to the Cu(111) facet, and the binding on the Cu(111) facet is referenced to the gas phase without showing the error. The observed differences in binding energies between the facets are minor for both the ΔE_{CO^*} and ΔE_{H^*} energies. All the Cu facets bind CO*, while they do not have underpotential deposited H*, meaning that a potential below 0 V_{RHE} has to be applied to adsorb hydrogen. This provides an explanation for why Cu is the only pure metal that can catalyze the formation of hydrocarbons.[21] However, it does not explain the CC coupling, as the CC coupling intermediate OCCO* [9,14] is not stable in vacuum calculations. To investigate how water affects the electrochemical interface and thereby the key intermediates, CO*, the proposed OCCO*, and H*, we carry out AIMD simulations of an aqueous phase in contact with the Cu facets.

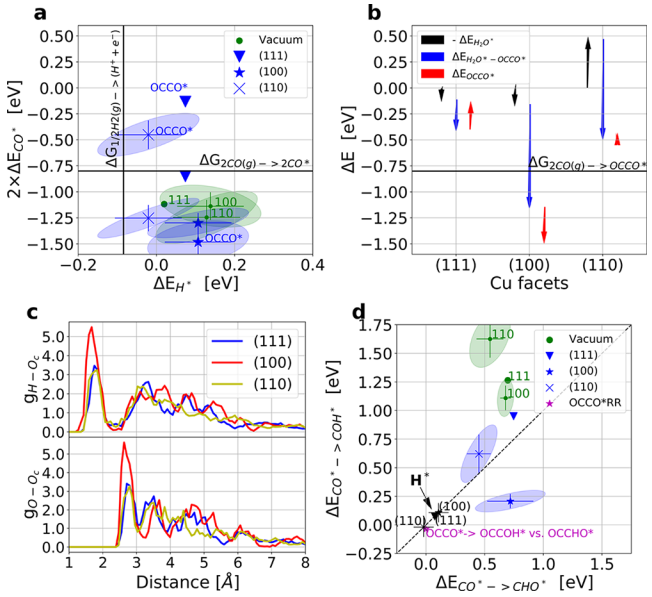

Figure 2. (a) Trend study of the 2CO*, OCCO*, and H* binding energies in the electrolyte (blue markers) for Cu(111), Cu(100), and Cu(110), showing the unique ability of the Cu(100) facet to stabilize OCCO* relative to 2CO* in the aqueous electrolyte. (b) The three contributions to the interface OCCO* binding energy: water binding to the facets, water binding to the OCCO* facets, and the OCCO* vacuum binding energy. It can be seen that the presence of the OCCO* results in a significant change in hydrophilic properties of the water binding to the Cu(100) facet. (c) Pair correlation function around the oxygen atoms of the OCCO* intermediate. This shows that the Cu(100) facet has a higher peak for both water oxygen and hydrogen neighbors, as compared to the other facets. The higher peaks can be interpreted as a more well-ordered water structure stabilized by hydrogen bonding. (d) Protonation energy map for the protonation of CO* (blue markers), OCCO* (pink marker), and H* (black marker). The OCCOH* protonation is more favorable than the reaction $H^+ + e^-$ → H*, which explains the experimental observation of C_2H_4 prior to hydrogen evolution on Cu(100). Binding energy functional error ellipses obtained from single-point vacuum BEEF−vdW ensemble calculations referenced to Cu(111).

From these calculations we obtain ensembles of water structures of the interface region including these intermediates. This approach ensures that the interaction between the electrolyte and the intermediates (either stabilization or destabilization) does not depend on the specific choice of water structure (see Methods section for calculation of binding energies). Snapshots of the OCCO* intermediate and the nearest water molecules on the different facets are shown in Figure S15. Single-point BEEF-vdW vacuum calculations are carried out on top of the AIMD structure without water to obtain functional error ensembles of the binding energies.

The interface calculations show that the proposed OCCO* is stable only on the Cu(100) facet, while on both the Cu(111) and the Cu(110) facets the intermediate is unstable and can be held together only by applying a spring force during the AIMD simulations. Furthermore, we observe that CO* in the aqueous electrolyte is stable for all the Cu facets and the binding energies of both CO* and H* in water are comparable with the calculated binding energies in a vacuum.

The results of the interface AIMD calculations thus show distinct differences from the vacuum calculations, where the OCCO* intermediate is unstable on all facets. The difference in the stabilization effect cannot arise only from the specific

binding site, since the vacuum calculations on Cu(100) should then also have stabilized OCCO*. Previous investigations have shown a stable OCCO* by adding charge in the calculation,[9] using a constant electrode potential method and a dielectric implicit solvent model,[29,30] or using a protonated water layer.[10,31] Here, it is thus remarkable that the explicit aqueous phase without additional charge near the Cu(100) surface has such a stabilization effect on the OCCO*.

Whereas Figure 2a shows the obtained binding energy, the binding energy in Figure 2b shows how the OCCO* binding can be split into three contributions by calculating constrained structures of the OCCO*, water layer, and water layer in contact with the OCCO* surface as follows:

Figure 2a:

$$\langle \Delta E_{\mathrm{OCCO}^*} \rangle = \langle E_{\mathrm{OCCO}^*,\mathrm{H_2O}^*} \rangle - \langle E_{\mathrm{H_2O}^*} \rangle - 2E_{\mathrm{CO(g)}}$$

Figure 2b:

$$\langle \Delta E_{\mathrm{OCCO}^*} \rangle = \underbrace{\Delta E_{\mathrm{OCCO}^*}}_{\text{vacuum binding}} + \overbrace{\underbrace{\Delta E_{\mathrm{H_2O}^*-\mathrm{OCCO}^*}}_{\text{water binding to OCCO* surface}} - \underbrace{\Delta E_{\mathrm{H_2O}^*}}_{\text{water binding}}}^{\text{change in water binding due to OCCO*}}$$

where

$$\Delta E_{\mathrm{OCCO}^*} = \langle E_{\mathrm{OCCO}^*} \rangle - E_* - 2E_{\mathrm{CO(g)}}$$

$$\Delta E_{\mathrm{H_2O}^*-\mathrm{OCCO}^*} = \langle E_{\mathrm{OCCO}^*,\mathrm{H_2O}^*} \rangle - \langle E_{\mathrm{H_2O}} \rangle - \langle E_{\mathrm{OCCO}^*} \rangle$$

$$\Delta E_{\mathrm{H_2O}^*} = \langle E_{\mathrm{H_2O}^*} \rangle - \langle E_{\mathrm{H_2O}} \rangle - E_*$$

and $\langle E_{\mathrm{H_2O}} \rangle$ is the energy for water structures without the metal facet.

Figure 2b shows how each of these three contributions gives the OCCO* binding energies in Figure 2a. For Cu(111) and Cu(100), the water ($\Delta E_{\mathrm{H_2O}^*}$) does not bind, while the water in contact with the more open facet, Cu(110), binds strongly. Changing the surface by having the OCCO* in contact with the water gives in all cases a stabilization of the water; in particular, for Cu(100) and Cu(110) this water stabilization is ~1 eV. The difference in water binding energy with and without OCCO* reflects a change in hydrophilic properties of the facets relative to each other, and adding up the minor OCCO* vacuum binding energy, one obtains the interface binding energy of OCCO*. Significantly, this shows that OCCO* is only stable on Cu(100) due to the change in the hydrophilic properties of the surface when OCCO* is adsorbed, with OCCO* having better adsorption energy in a vacuum to the Cu(111) and Cu(110) facets.

Figure 2c investigates aspects of the solvation structure of water around the intermediate. It shows the radial distribution function of hydrogen ($g_{\mathrm{H-O_c}}$, top) and oxygen ($g_{\mathrm{O-O_c}}$, bottom) atoms around the oxygen atoms of the OCCO* intermediate for each of the three Cu facets. The graphs show how water molecules near the different facets orient, order, and stabilize the OCCO* intermediate by means of hydrogen bonding, clearly visible in the peaks in $g_{\mathrm{H-O_c}}$ at around 1.7−1.8 Å. The significantly higher values of the first maxima in both the oxygen and the hydrogen pair correlation functions show that solvation of the OCCO* intermediate in the Cu(100) ensemble is stronger as compared to that in the Cu(111) and Cu(110) facets. This trend reflects the trend in the energetics shown in Figure 2a,b.

The ability to bind CO*, while simultaneously not binding H_{upd}, is the requirement a potential catalyst for CO reduction must fulfill.[21] However, Cu catalysts are expected to be able to reduce (protonate) CO* on all facets, and protonate OCCO* on the Cu(100) facet.

Figure 2d shows a protonation energy map with carbon protonation and oxygen protonation on the x and y axes, respectively. Interestingly, carbon protonation to the CHO* intermediate in the electrolyte simulations is very similar to that in the vacuum calculation, while oxygen protonation to COH* is significantly stabilized by the electrolyte environment.[17] This shows the effect of having an −OH bond reaching out into the electrolyte, which can form hydrogen bonds with the surrounding aqueous phase. The most stabilized CO* protonation to COH* occurs on the Cu(100) facet. Furthermore, calculated H* binding energies in the electrolyte are shown by black markers on the diagonal, to indicate that these are stabilized more in the aqueous interface than the CO* protonation products. Hence, CO* protonation cannot account for the earlier onset potential for CC coupling as compared to hydrogen evolution reaction (HER), as observed experimentally. Only on the Cu(100) facet is protonation of the OCCO* intermediate to OCCOH* or OCCHO* more favorable than H* adsorption. The functional dependence of the conclusion shows that only 5 out of 2000 functionals from the BEEF-vdW ensemble give H* adsorption prior to OCCHO*, while 0 out of 2000 have H* adsorption prior to OCCOH*. Thus, the observation that OCCO* is protonated prior to HER is robust within the DFT-GGA approximation.

To obtain a full reaction pathway going from CO(g) to C_2H_4(g), multiple protonated intermediates are calculated inside the aqueous interface model (see Figure S11). Relevant intermediates are selected, and by the use of the GCHE scheme (see Methods section), the energy of each AIMD state is set with respect to potential and pH, which enables one to obtain the free energy diagram as both potential- and pH-dependent. Figure 3 presents the free energy diagram at pH = 13 and for three characteristic U_{RHE} potentials as derived from the GCHE energy of the states shown in the inset. The inclusion of the potential-independent CO*-to-OCCO* dimer barrier in the calculation is shown in Figure S13, and a graph showing HER under similar conditions is shown in Figure S12. We remark that the free energy diagram provides realistic states under the conditions of the electrolyte (pH, concentrations, etc.) and electrochemical barriers for the free energy diagram would be preferable. Schemes have been developed[32] assuming constant interface structures. However, there is not a method to obtain electrochemical barriers between realistic states at constant electrochemical conditions. The three characteristic U_{RHE} potentials chosen are the equilibrium potential for CO(g) to C_2H_4(g) (blue), the potential at which the potential-dependent step is still rate-determining (red), and the potential at which all charge-transfer steps are exergonic (yellow). The combination of a small OCCO* dimer barrier and a possible protonation at very low overpotential provides an explanation for the first question asked in this work, why the formation of C_2H_4 is possible at a low overpotential on Cu(100), before H_2 formation occurs.

However, it does not explain the experimental change in onset potential, which is observed to be dependent on the nature of the

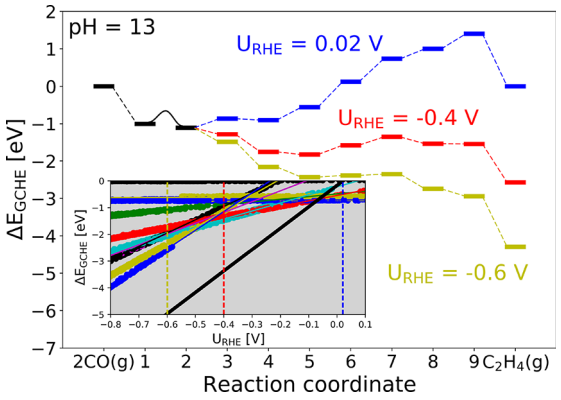

Figure 3. Free energy diagram from CO(g) to C_2H_4(g) at pH = 13 and at three characteristic U_{RHE} potentials: the equilibrium potential for CO(g) to C_2H_4(g) (blue), the potential at which the potential-dependent step is still rate-determining (red), and the potential at which all charge-transfer steps are exergonic (yellow). The three different U_{RHE} potentials show that the formation of C_2H_4 is possible at a low overpotential on Cu(100). The pH- and U_{RHE}-dependent free energy diagram is obtained by combining AIMD simulations of possible intermediates and setting the energy of each state by utilizing the GCHE scheme as a function of pH and potential as shown in the inset (see Figure S11 for more intermediates). The points in the inset correspond to AIMD states, with each color representing relevant intermediates, and the solid lines are fitted to the AIMD states, while dashed lines show the three characteristic U_{RHE} potentials. Further, the potential-independent CO*-to-OCCO* barrier is almost negligible, shown in black and calculated as shown in Figure S13.

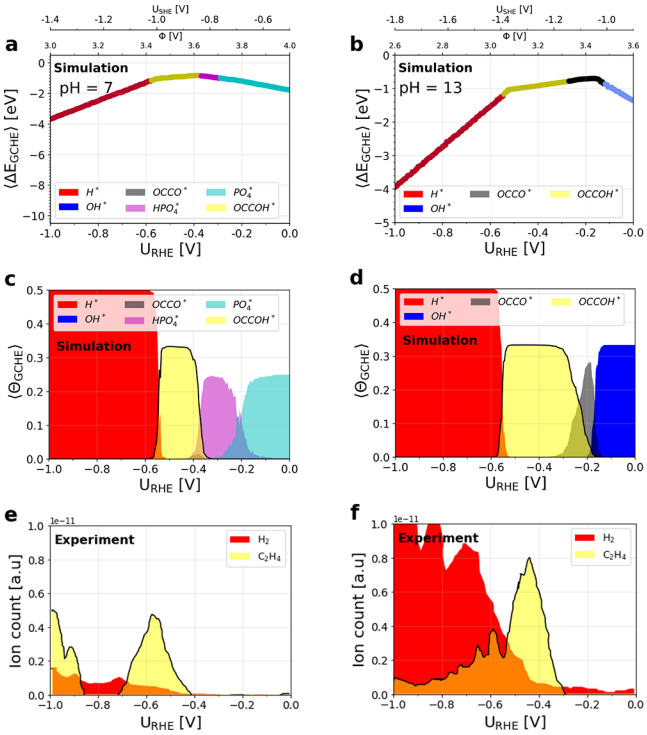

Figure 4. (a, b) Interface phase diagrams calculated by Boltzmann weighting of the energies obtained from the GCHE scheme to give the most stable configurations as a function of pH and potential. (c, d) Coverage obtained from the interface phase diagrams, which is compared to the experimental results below in (e, f). A clear correlation can be seen between the experimental C_2H_4 mass spectrometry signal and the region where the OCCOH* intermediate covers the surface according to our calculations. The C_2H_4 mass spectrometry tail tracing the H_2 signal, shown by the orange overlap of the red and yellow colors, represents a combination of H* and OCCOH* at the interface, which has not been calculated. Note that the absolute experimental mass spectrometry signal rates cannot be obtained, and the calculations yield only coverages without considering the forward reactions in steady-state conditions. Figure S6 show both electrolytes at opposite pH. Experimental data are adapted from ref 14.

electrolyte and on pH.[14] To unravel this further, we investigate the electrochemical properties of the interface.

Electrochemical Interface Effects on CC Coupling on the Cu(100) facet. Next, we will try to answer the second question of why the C_2H_4 evolution changes with electrolyte and pH. To this end, we perform AIMD simulations of the interface of aqueous electrolyte with Cu(100), which is covered with H* and OH* from zero up to half coverage (n/N, where n is the number of protons added or subtracted and N is the number of surface atoms in the unit cell). Furthermore, we simulate electrolytes with single $H_xPO_4^*$ anions as well as OCCO* and OCCOH* species adsorbed at the surface. From each of these AIMD simulations we save the energy and work function from each state to employ the GCHE scheme[22,23] (see Methods section).

The AIMD results together with eqs 1 and 2 allow us to represent $\langle \Delta E_{GCHE} \rangle$ as a function of U_{RHE} in a phase diagram at pH = 7 with phosphate ion configurations, and at pH = 13 for the aqueous electrolyte in Figure 4a,b. The standard hydrogen electrode (U_{SHE}) and work function (ϕ) potential scales are included above the two frames, which show how the two potential scales relate to the reversible hydrogen electrode (U_{RHE}) scale seen below the frames. Furthermore, each bin with an intermediate coverage above 0.1 of one of the OCCO*, OCCOH*, and $H_xPO_4^*$ adsorbates has been assigned the respective color of the legend. The results in the phase diagrams (Figure 4a,b) represent raw data of the most stable states under the conditions. The slope corresponds to the charge at the surface, while the coverages at the surface may not exactly be similar to the charge. Hence we also display the coverages.

The coverages $\langle \Theta_{GCHE} \rangle$ of each species of interest are plotted as a function of U_{RHE} (Figure 4c,d) for the phosphate buffer and the aqueous electrolyte, respectively. This result strikingly explains the onset potential change for the C_2H_4 mass spectrometry signal on the Cu(100) facet in the phosphate buffer experiment at pH = 7 and in the sodium hydroxide experiment at pH = 13 by comparison with the experimental reaction mass spectrometry signals shown in Figure 4e,f on the same potential scale (data from Schouten et al.[14]).

The simulated coverage of OCCOH* in each electrolyte falls into the potential window where CC coupling toward C_2H_4 takes place, but before the H* coverage increases, which results in a combined H_2 and C_2H_4 rate signal. In this latter region, the calculated combination of OCCOH* and H* would only approximate the C_2H_4 mass spectrometry signal and still not explain the absolute observed mass spectrometry signal of C_2H_4 compared to H_2, as this may also depend on the role of the protonation kinetics.[33,34] In fact, the reaction rate depends not only on the thermodynamic window of a stable OCCOH* intermediate but also on the nature of the cations present, as was recently shown experimentally.[16,35]

Comparing the thermodynamic windows of the two electrolytes in Figure 4c,d shows the main shortcomings of employing a phosphate buffer electrolyte. Here, the simulations show that the Cu(100) facet is covered by HPO_4^* anions up to high overpotentials, whereas in the aqueous electrolyte the OH*

coverage is the limitation for CC coupling at lower overpotential. Thus, the energetic limitation for CC coupling is merely an electrolyte counterion-dependent property and not a pH-dependent property. In Figure S6 data for the phosphate electrolyte at pH = 13 and the water electrolyte at pH = 7 are shown, demonstrating that phosphate species become unstable at alkaline pH. Despite the uncertainties with respect to reference (see Figure S8), the phosphate electrolyte result is in line with experiments by Hori et al.[36−38] and Kortlever et al.[39]

These results also allow us to investigate the CO_2 reduction reaction (CO2RR) interface, which is in constant equilibrium with carbonate species. The carbonate anions could block the Cu facets, which consequently would limit the CO2RR at low overpotentials. Figure 5 shows the calculated phase diagram and

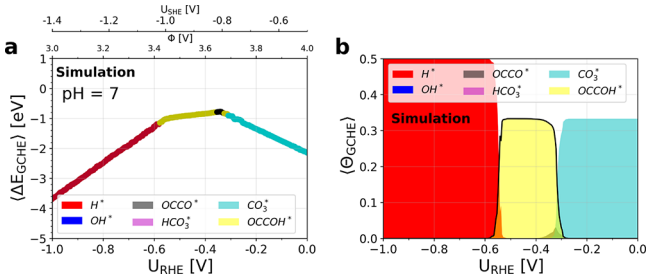

Figure 5. (a) Interface phase diagram calculated by Boltzmann weighting of the energies obtained from the GCHE scheme to give the most stable configurations as a function of pH and potential. (b) Coverage obtained from the interface phase diagrams, showing that CO_3^* anions are more stable than OH* on the surface but still less poisoning than phosphate. This result indicates that overpotential differences between CORR in alkaline electrolyte (NaOH, KOH, ...) and CO2RR in bicarbonate electrolyte are due to a carbonate poisoned surface.

coverage including HCO_3^* and CO_3^* species for Cu(100) at pH = 7, and assuming a constant chemical potential of carbonate species as is in the solution. Indeed, this shows that carbonate species cover the surface until an overpotential larger than that of OH* intermediates found in alkaline electrolytes (NaOH, KOH, ...), while the carbonate does not block the surface as strongly as a phosphate anion. Although the change from OH* anion to CO_3^* is smaller than the experimental results comparing CO2RR in bicarbonate and CO reduction in KOH, it does reflect the trends observed for CO2RR and CORR comparison studies,[40] and further it explains how the construction of an abrupt KOH interface can lower the CO2RR overpotential.[41]

Additionally, we can understand why it is difficult to experimentally confirm the formation of OCCO* dimers. A certain minimum overpotential is necessary to remove anions or OH* intermediates from the surface while not protonating the OCCO* dimer, which, as can be seen, is thermodynamically almost impossible. In the aqueous electrolyte, the OCCO* dimer is present just after OH* has left the surface; however, with a similar probability of finding the OCCOH* intermediate, the OCCO* has a negligible lifetime on the surface. Observation of the OCCOH* intermediate has indeed been confirmed experimentally at low overpotential in a lithium hydroxide electrolyte,[42] which also agrees with our simulation results.

Cation Effects in the Electrochemical Interface on CC Coupling on the Cu(100) Facet. Recently, increased interest has been devoted to studying how cations may affect CO_2/CO reduction toward different products.[16,35] Here, we will show how our methodology can be used to investigate the questions of how the C_2H_4 evolution thermodynamically depends on the nature of cations and, in turn, how the cations affect the electrochemical interface.

Simulations are performed with charge neutral Na, K, and Cs atoms added to our Cu(100) interface simulations, and quantum mechanics determines if these atoms become cations or molecules. Hence, we refer to Na, K, and Cs as cations. These cations are chosen so that the simulations can be directly compared with recent experiments on the Cu(100) facet with different cations by Gallent et al.[16] Since the addition of cations to AIMD simulations increases calculation time significantly, we sample as few states as possible.

Figure 6a shows the cation position density in the interface model as a function of the Cu(100) surface, as illustrated in the

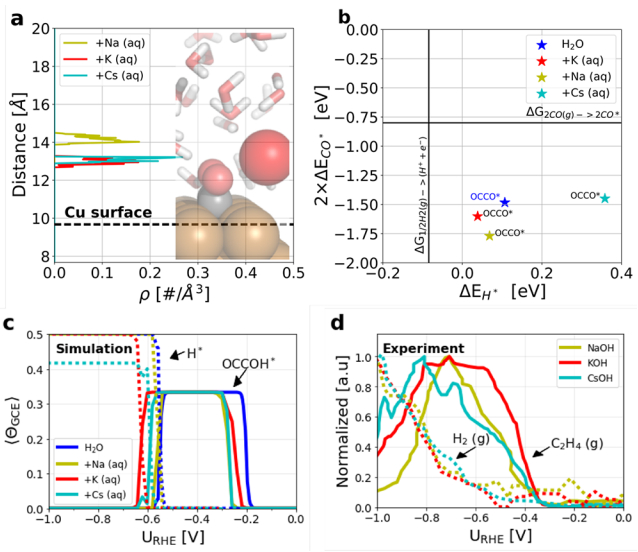

Figure 6. (a) Cation position density in the interface model, showing that the cation is approximately 3 Å from the surface and close to the OCCO* intermediate illustrated by the figure insert. (b) Trend study approach for the OCCO* and H* binding energies in different alkali metal electrolyte solutions on the Cu(100) facet. The energies show only minor dependencies on the nature of the cation introduced in the interfacial region. (c) Coverage plots of OCCOH* and H* intermediates, which can be compared with the experimental results of C_2H_4 and H_2 mass spectrometry signal in (d), respectively. The simulations show that different cation electrolytes do not affect the OCCOH* and H* intermediates significantly, which corresponds well with the normalized experiments. Experimental data are adapted from ref 16, which had a constant offset by 0.2 eV as compared with ref 14; this is discussed in the text.

inset. The different cations are shown to be in the first water layer, close to the OCCO* intermediate. However, remarkably, the cation close to the intermediates does not change the thermodynamic binding energy of the intermediates. In Figure 6b, the relevant energy data from the cation studies are added to our energetic trend study framework.[21] This shows that different cations do not change the binding energy of OCCO* and H* significantly as compared to the stabilization through the presence of water. This indicates that the cations probably do not play an important role in the thermodynamics of CC coupling. However, we investigate the potential window of C_2H_4 evolution in the presence of the cations to compare with experiments and the simulations of pure aqueous electrolyte.

To add the cation electrolyte states in equilibrium with electrons, protons, and ions, we apply the GCHE scheme in a

modified form to include the ions (see Methods section). From this treatment, we again plot the coverage plots of OCCOH* and H* with and without cations in Figure6c, allowing the comparison of trends obtained from the simulation with experimental trends on the Cu(100) facet (shown in Figure6d).

We note that the experimental Cu(100) facet studies by Schouten et al.[14] and Gallent et al.[16] show two main differences (compare Figure 4f with Figure 6d). First, the potential window of C_2H_4 mass spectrometry signal is much broader in the more recent work, although similar for the different cations, as compared to the earlier experiments. Second, the H_2 and C_2H_4 evolution onset potential is shifted negatively in the recent experiments. This indicates that reproducibility of these types of experiments is difficult to achieve, and after discussion with the authors, we rely on the comparison of the phosphate buffer and NaOH electrolyte simulations with the work by Schouten et al.[14] and the comparison of the cation simulations with the work by Gallent et al.[16]

Comparing our simulations in Figure 6c for the different cations, we do not observe significant differences as compared to the aqueous electrolyte simulations. The OCCOH* coverage is limited first by an OH* coverage at low overpotential and by H* at high overpotential, and only negligible differences are seen between the different cations. Comparing with the experiments in Figure 6d, we do observe an offset in both HER and C_2H_4 signal; however, we accept this offset based on the discussion of experiments (the offset could be fitted by shifting the H_2 energy as in Figure S7). Overall it seems that, for HER and C_2H_4, the thermodynamics are unchanged by different alkali metal electrolytes, while the cation may affect the kinetics of the protonation.

DISCUSSION

In this work we have shown, using Ab Initio Molecular Dynamics (AIMD) simulations, how the CO reduction intermediates are affected by the presence of an aqueous phase. We find that, in the aqueous electrolyte, the OCCO* intermediate is stable only on the Cu(100) facet, while the CO* and H* simulations for all facets show only minor differences from the respective vacuum calculations. Investigating the water stabilization of OCCO* on the Cu(100) facet shows that the aqueous phase is more structured and that the hydrophilic properties are changed significantly by the presence of the OCCO* intermediate as compared to those on the other facets.

To move beyond the binding of CO* and OCCO* on the Cu facets, we investigate the species obtained by a first protonation step. We observe the trend that the COH* intermediate on all facets is stabilized significantly as a consequence of the solvation of the −OH group by water, whereas the CHO* intermediate is unaffected by the electrolyte. However, none of these protonations is energetically favorable at potentials prior to H* intermediate adsorption. Only the protonation of OCCO* to OCCHO* or OCCOH* occurs at potentials prior to H* adsorption; here, the adsorption of the OCCOH* is most favorable. Hence, the special nature of the aqueous interface on the Cu(100) allows not only stabilization of the OCCO* intermediate but also an earlier protonation than the potential needed for formation of H* intermediates on the surface. This explains the occurrence of CC coupling prior to HER on the Cu(100) facet.

We demonstrate, by using multiple AIMD simulations together with the GCHE scheme, that the origin of the changed onset potential is not a pH effect but rather an electrolyte counterion effect. By direct comparison with experiments, we show that the limiting factor in the phosphate buffer electrolyte is the coverage of HPO_4^* anions, while in the alkali metal hydroxide electrolyte the limitation may be the coverage of OH* intermediates or the latter reduced OCCO* intermediate. To compare our CORR results with those of CO2RR carried out in bicarbonate solution, we also show that CO_3^* anions poison the surface more strongly than OH*, but less strongly than a phosphate anion. This indicates that overpotential differences in CO and CO_2 reduction reaction experiments on measured products may be a result of anion poisoning.

The simulations of the interface region with solvated Na, K, and Cs ions make it possible to study the trends in C_2H_4 and H_2 production related to the different cations. It is found that the nature of the cation has only a minor influence on the thermodynamic window, corresponding well with experiments. Consequently, cations present in the interface region are likely to affect only rate properties, and not the thermodynamically defined adsorption energies.

Summarizing these investigations, we can list the requirements of the catalytic interface to produce CC products in electrochemical CO reduction:

(1) no underpotential-deposited hydrogen (H_{upd})
(2) binding of CO*
(3) OCCO* stable relative to CO*
(4) OCCO* protonated at potentials prior to HER
(5) low coverage of spectators

Understanding the electrochemical interface at this level provides a deep understanding of the properties to gain a high amount of CC bonded products from CO reduction. We believe that this methodology can elucidate such complex situations to give us a fundamental understanding, and it illustrates a shift in simulation techniques for electrochemistry from vacuum binding energies to more realistic electrocatalytic interface simulations.

METHODS

Generalized Computational Electrode (GCE). In order to generate the interface phase diagrams from our AIMD trajectories containing energy and work function, we apply the Generalized Computational Hydrogen Electrode (GCHE) scheme[22,23] in two different versions: first for aqueous electrolyte simulation and with the addition of phosphorus or carbonate states, and second in a modified version to include the cations.

The pertinent GCHE equation for our phosphorus and aqueous electrolyte investigations defines the energy of each state of the AIMD configurations for a given potential and pH as

$$\Delta E_{\mathrm{GCHE}}(n, p, q, \phi_{e^-}, \mathrm{pH}) = E(n, p, q, \phi_{e^-}) - \langle E(\{n, p, q\} = 0)\rangle - p\mu_{\mathrm{CO(g)}} - q\mu_{\mathrm{H_3PO_4(aq)}} - n\frac{1}{2}\mu^0_{\mathrm{H_2}} - n\overbrace{(\phi_{\mathrm{SHE}} - \phi_{e^-} - 2.3k_{\mathrm{B}}T\,\mathrm{pH})}^{eU_{\mathrm{RHE}}} \quad (1)$$

where $p = \{0, 1, 2\}$, $q = \{0, 1\}$, and $n = \{-6, .., 6\}$. Here the energy, ΔE_{GCHE}, is a function of the number of protons n removed or added, the number of CO adsorbates p, the number of H_3PO_4(aq) q, the work function ϕ_{e^-}, and pH (U_{RHE}). μ denotes the chemical potential of molecules, ϕ_{SHE} is the defined standard hydrogen electrode potential of 4.4 V on the absolute scale,[43] k_{B} is Boltzmann's constant, T is the absolute temperature, and $\langle E(\{n, p, q\} = 0)\rangle$ is the reference energy. The energies obtained in this way are depicted in Figure S5, and the bicarbonate anions can be included in a similarly way. The thermodynamics data used for phosphate are shown in Tables S1−S4 and for bicarbonate in Tables S5−S7. References made in this way carry uncertainties with respect to the entropy of the species in the interface,

functional errors, and basis set errors, and they generally rely on absolute values as compared to trend schemes.

However, in order to obtain the energy and coverage of the interface at the specific conditions determined in eq 1, all the GCHE energy states are Boltzmann-weighted by binning the data within a bin of chosen size, as

$$\langle A \rangle = \frac{1}{Z}\sum_{i=1}^{N} A_i \exp\left(\frac{-\Delta E_{\mathrm{GCHE}}(n, p, q, \phi_{e^-}, \mathrm{pH})_i}{k_{\mathrm{B}}T}\right),$$
$$A = \{\Delta E_{\mathrm{GCHE}}, \Theta_{\mathrm{GCHE}}\} \quad (2)$$

where Z is the partition function, N is the total number of states in the bin, and $\langle A \rangle$ is the property of interest, in this case the energy $\langle \Delta E_{\mathrm{GCHE}} \rangle$ and the coverage $\langle \Theta_{\mathrm{GCHE}} \rangle$.

The specific GCHE equation for the cation investigations carried out here applies an additional term to define the energy of each state from the AIMD configurations as a function of ion concentration, potential, and pH as

$$\Delta E_{\mathrm{GCE}}(n, p, I, \phi_{e^-}, \mathrm{pH}) = E(n, p, I, \phi_{e^-}) - \langle E(\{n, p, I\} = 0) \rangle$$
$$- p\mu_{\mathrm{CO(g)}} - n\frac{1}{2}\mu^0_{\mathrm{H_2}} - n\overbrace{(\phi_{\mathrm{SHE}} - \phi_{e^-} - 2.3k_{\mathrm{B}}T\,\mathrm{pH})}^{eU_{\mathrm{RHE}}}$$
$$- I\mu^0_{\mathrm{ion(s)}} - I\overbrace{(\phi_{\mathrm{ion}} - \phi_{e^-} + k_{\mathrm{B}}T\,\log M)}^{eU_{\mathrm{ion}}} \quad (3)$$

where $p = \{0, 1, 2\}$, $I = \{0, 1\}$, and $n = \{-6, ..., 6\}$. Here the energy ΔE_{GCE} now denotes a generalized computational electrode, which is a function of the number of protons n removed or added, the number of CO molecules p, the work function ϕ_{e^-}, pH (U_{RHE}), and the number of ions I added to the interface and which have ionization potential on the absolute potential scale ϕ_{ion} and a concentration M. Again, $\langle E(\{n, p, I\} = 0) \rangle$ is the reference energy, and the GCE energy states are Boltzmann-weighted to obtain the interface phase diagram and coverage plots in Figure S9.

Computational Details. Atomic structures were built with ASE.[44] The vacuum metal facet structures are composed of face-centered cubic (3×3×4) unit cells, with the two bottom layers fixed. The water interface models are constructed as orthogonal (3×4×3), (3×4×3), and (2×4×3) unit cells for the (111), (100), and (110) copper facets, respectively, to obtain similar *xy* plane interface areas of the unit cells. Each water interface model consists of 3 water layers with a total of 24 H_2O molecules, which are allowed to move freely during the simulation. An additional hexagonal water layer on top of the mobile aqueous phase is also kept fixed in order to keep the water density of the interface model constant and close to that of pure water. When atoms (protons or intermediates) are added and subtracted, the top water layer remains unchanged. Although the water interface models are more realistic, they still suffer from limitations due to thickness of water, area of unit cell, periodicity of cell, and more.

The electronic structure calculations are carried out at the Generalized Gradient Approximation Density Functional Theory (GGA-DFT) level with the projector-augmented wave method as implemented in GPAW.[45] Different levels of electronic structure calculation were employed: (1) BEEF-vdW[27,28] functional calculations are carried out for vacuum binding energies to estimate functional-dependent errors and using (4×4×1) k-points and a 0.18 Å grid spacing. (2) The water/copper interface is modeled by AIMD at a constant temperature of 300 K (using Berendsen[46] NVT dynamics, with a time step of 0.5 fs and a time temperature cooling constant of 200 fs) as implemented in GPAW. In Figures S1 and S3, AIMD results are shown from the beginning until an (on average) constant total energy is achieved. To achieve thermal equilibration and a sufficient number of states for the GCHE approach, the electronic structure calculations are carried out by RPBE[47] calculations in LCAO mode, with a grid spacing of 0.18 Å at the gamma point. From these AIMD ensembles, we calculate the binding energy of, e.g., CO according to

$$\Delta E_{\mathrm{CO}*} = \langle E_{\mathrm{CO}*} \rangle - \langle E_* \rangle - E_{\mathrm{CO(g)}} \quad (4)$$

where $\langle\ \rangle$ means it is the average potential energy of the equilibrated ensemble obtained, as shown in Figure S3 and presented in Figure 2a as the blue markers for each facet.

To determine whether the conclusions from the AIMD are robust with respect to the level of calculation, and to reject conclusions based on basis set and k-point errors, a selected set of fixed AIMD configurations is considered with LCAO settings and high finite difference settings; see Figure S4a. The data show an expected constant offset and acceptable deviations from the mean. Further, the systematic work function error of the LCAO calculations is estimated by comparing with finite difference calculations, as shown in Figure S4b. This yields a mean error of ∼0.4 eV, which is slightly higher than previously reported values, which were around ∼0.3 eV. However, the calculated offset for the LCAO work function only leads to the production of states having an incorrect potential; correcting for the work function error only changes the distribution in a minor way, and the results can be assumed almost unaffected by this. Finally, as the LCAO method suffers from basis set superposition errors, the molecular vacuum energies for the LCAO calculations are determined by adding ghost states corresponding to the basis set of the calculated interface unit cell. With the ghost states, the vacuum binding energies in the LCAO mode for H* are still determined to have a constant offset as compared to the BEEF-vdW calculation; consequently, a 0.2 eV correction is added to the H* binding energy, thereby matching the Cu(111) facet binding energies at both levels of electronic structure code. After correcting the H* energy, we also test the robustness of our main findings by changing the H_2(g) energy by ±0.5 eV in Figure S7 and robustness of the H_3PO_4(aq) reference by ±0.5 eV in Figure S8.

Data Availability. Atomic structures and interface models together with databases and analysis scripts are available on our group's web page http://nano.ku.dk/english/research/theoretical-electrocatalysis/katladb/. Using the thermalized water systems available there can significantly reduce the calculation time for thermalization of future AIMD investigations.

AUTHOR INFORMATION

Corresponding Author

*jan.rossmeisl@chem.ku.dk

ORCID

Martin H. Hansen: 0000-0003-0818-1515

Jan Rossmeisl: 0000-0001-7749-6567

Notes

The authors declare no competing financial interest.

ACKNOWLEDGMENTS

This work was supported by Climate-KIC under the EnCO$_2$re project, the Carlsberg Foundation (grant CF15-0165), and the Innovation Fund Denmark (grand solution ProActivE 5124-00003A). E.S. thanks the University of Copenhagen for its hospitality during his sabbatical leave from Universtity of Duisburg-Essen.

REFERENCES

(1) Chu, S.; Cui, Y.; Liu, N. The path towards sustainable energy. *Nat. Mater.* **2017**, *16*, 16.

(2) Obama, B. The irreversible momentum of clean energy. *Science* **2017**, *355*, 126−129.

(3) Liu, M.; et al. Enhanced electrocatalytic CO2 reduction via field-induced reagent concentration. *Nature* **2016**, *537*, 382.

(4) Chen, Y.; Li, C. W.; Kanan, M. W. Aqueous CO_2 Reduction at Very Low Overpotential on Oxide-Derived Au Nanoparticles. *J. Am. Chem. Soc.* **2012**, *134*, 19969−19972.

(5) Ju, W.; Bagger, A.; Hao, G.-P.; Varela, A. S.; Sinev, I.; Bon, V.; Roldan Cuenya, B.; Kaskel, S.; Rossmeisl, J.; Strasser, P. Understanding activity and selectivity of metal-nitrogen-doped carbon catalysts for electrochemical reduction of CO2. *Nat. Commun.* **2017**, *8*, 944.

(6) Gao, S.; Lin, Y.; Jiao, X.; Sun, Y.; Luo, Q.; Zhang, W.; Li, D.; Yang, J.; Xie, Y. Partially oxidized atomic cobalt layers for carbon dioxide electroreduction to liquid fuel. *Nature* **2016**, *529*, 68.

(7) Bagger, A.; Ju, W.; Varela, A.; Strasser, P.; Rossmeisl, J. Single site porphyrine-like structures advantages over metals for selective electrochemical CO_2 reduction. *Catal. Today* **2017**, *288*, 74−78.

(8) Peterson, A. A.; Abild-Pedersen, F.; Studt, F.; Rossmeisl, J.; Nørskov, J. K. How copper catalyzes the electroreduction of carbon dioxide into hydrocarbon fuels. *Energy Environ. Sci.* **2010**, *3*, 1311−1315.

(9) Calle-Vallejo, F.; Koper, M. T. M. Theoretical Considerations on the Electroreduction of CO to C2 Species on Cu(100) Electrodes. *Angew. Chem., Int. Ed.* **2013**, *52*, 7282−7285.

(10) Montoya, J. H.; Shi, C.; Chan, K.; Nørskov, J. K. Theoretical Insights into a CO Dimerization Mechanism in CO_2 Electroreduction. *J. Phys. Chem. Lett.* **2015**, *6*, 2032−2037.

(11) Li, C. W.; Ciston, J.; Kanan, M. W. Electroreduction of carbon monoxide to liquid fuel on oxide-derived nanocrystalline copper. *Nature* **2014**, *508*, 504−507.

(12) Mistry, H.; Varela, A. S.; Bonifacio, C. S.; Zegkinoglou, I.; Sinev, I.; Choi, Y.-W.; Kisslinger, K.; Stach, E. A.; Yang, J. C.; Strasser, P.; Cuenya, B. R. Highly selective plasma-activated copper catalysts for carbon dioxide reduction to ethylene. *Nat. Commun.* **2016**, *7*, 12123.

(13) Verdaguer-Casadevall, A.; Li, C. W.; Johansson, T. P.; Scott, S. B.; McKeown, J. T.; Kumar, M.; Stephens, I. E. L.; Kanan, M. W.; Chorkendorff, I. Probing the Active Surface Sites for CO Reduction on Oxide-Derived Copper Electrocatalysts. *J. Am. Chem. Soc.* **2015**, *137*, 9808−9811.

(14) Schouten, K. J. P.; Qin, Z.; Gallent, E. P.; Koper, M. T. M. Two Pathways for the Formation of Ethylene in CO Reduction on Single-Crystal Copper Electrodes. *J. Am. Chem. Soc.* **2012**, *134*, 9864−9867.

(15) Schouten, K. J. P.; Gallent, E. P.; Koper, M. T. M. Structure Sensitivity of the Electrochemical Reduction of Carbon Monoxide on Copper Single Crystals. *ACS Catal.* **2013**, *3*, 1292−1295.

(16) Pérez-Gallent, E.; Marcandalli, G.; Figueiredo, M. C.; Calle-Vallejo, F.; Koper, M. T. M. Structure- and Potential-Dependent Cation Effects on CO Reduction at Copper Single-Crystal Electrodes. *J. Am. Chem. Soc.* **2017**, *139*, 16412−16419.

(17) Herron, J. A.; Morikawa, Y.; Mavrikakis, M. Ab initio molecular dynamics of solvation effects on reactivity at electrified interfaces. *Proc. Natl. Acad. Sci. U. S. A.* **2016**, *113*, E4937−E4945.

(18) Naderian, M.; Groß, A. From single molecules to water networks: Dynamics of water adsorption on Pt(111). *J. Chem. Phys.* **2016**, *145*, 094703.

(19) Kristoffersen, H. H.; Vegge, T.; Hansen, H. A. OH formation and H2 adsorption at the liquid water-Pt(111) interface. *Chem. Sci.* **2018**, *9*, 6912−6921.

(20) Sakong, S.; Groß, A. The electric double layer at metal-water interfaces revisited based on a charge polarization scheme. *J. Chem. Phys.* **2018**, *149*, 084705.

(21) Bagger, A.; Ju, W.; Varela, A. S.; Strasser, P.; Rossmeisl, J. Electrochemical CO2 Reduction: A Classification Problem. *ChemPhysChem* **2017**, *18*, 3266−3273.

(22) Rossmeisl, J.; Chan, K.; Ahmed, R.; Tripkovic, V.; Bjørketun, M. E. pH in atomic scale simulations of electrochemical interfaces. *Phys. Chem. Chem. Phys.* **2013**, *15*, 10321−10325.

(23) Hansen, M. H.; Rossmeisl, J. pH in Grand Canonical Statistics of an Electrochemical Interface. *J. Phys. Chem. C* **2016**, *120*, 29135−29143.

(24) Hori, Y.; Murata, A.; Takahashi, R. Formation of hydrocarbons in the electrochemical reduction of carbon dioxide at a copper electrode in aqueous solution. *J. Chem. Soc., Faraday Trans. 1* **1989**, *85*, 2309−2326.

(25) Hori, Y.; Wakebe, H.; Tsukamoto, T.; Koga, O. Electrocatalytic process of CO selectivity in electrochemical reduction of CO2 at metal electrodes in aqueous media. *Electrochim. Acta* **1994**, *39*, 1833−1839.

(26) Kuhl, K. P.; Cave, E. R.; Abram, D. N.; Jaramillo, T. F. New insights into the electrochemical reduction of carbon dioxide on metallic copper surfaces. *Energy Environ. Sci.* **2012**, *5*, 7050−7059.

(27) Wellendorff, J.; Lundgaard, K. T.; Møgelhøj, A.; Petzold, V.; Landis, D. D.; Nørskov, J. K.; Bligaard, T.; Jacobsen, K. W. Density functionals for surface science: Exchange-correlation model development with Bayesian error estimation. *Phys. Rev. B: Condens. Matter Mater. Phys.* **2012**, *85*, 235149.

(28) Medford, A. J.; Wellendorff, J.; Vojvodic, A.; Studt, F.; Abild-Pedersen, F.; Jacobsen, K. W.; Bligaard, T.; Nørskov, J. K. Assessing the reliability of calculated catalytic ammonia synthesis rates. *Science* **2014**, *345*, 197−200.

(29) Goodpaster, J. D.; Bell, A. T.; Head-Gordon, M. Identification of Possible Pathways for C-C Bond Formation during Electrochemical Reduction of CO2: New Theoretical Insights from an Improved Electrochemical Model. *J. Phys. Chem. Lett.* **2016**, *7*, 1471−1477.

(30) Garza, A. J.; Bell, A. T.; Head-Gordon, M. Mechanism of CO2 Reduction at Copper Surfaces: Pathways to C2 Products. *ACS Catal.* **2018**, *8*, 1490−1499.

(31) Jiang, K.; Sandberg, R. B.; Akey, A. J.; Liu, X.; Bell, D. C.; Nørskov, J. K.; Chan, K.; Wang, H. Metal ion cycling of Cu foil for selective C-C coupling in electrochemical CO2 reduction. *Nat. Catal.* **2018**, *1*, 111−119.

(32) Skúlason, E.; Karlberg, G. S.; Rossmeisl, J.; Bligaard, T.; Greeley, J.; Jónsson, H.; Nørskov, J. K. Density functional theory calculations for the hydrogen evolution reaction in an electrochemical double layer on the Pt(111) electrode. *Phys. Chem. Chem. Phys.* **2007**, *9*, 3241−3250.

(33) Nie, X.; Esopi, M. R.; Janik, M. J.; Asthagiri, A. Selectivity of CO_2 Reduction on Copper Electrodes: The Role of the Kinetics of Elementary Steps. *Angew. Chem., Int. Ed.* **2013**, *52*, 2459−2462.

(34) Hussain, J.; Jónsson, H.; Skúlason, E. Calculations of Product Selectivity in Electrochemical CO2 Reduction. *ACS Catal.* **2018**, *8*, 5240−5249.

(35) Resasco, J.; Chen, L. D.; Clark, E.; Tsai, C.; Hahn, C.; Jaramillo, T. F.; Chan, K.; Bell, A. T. Promoter Effects of Alkali Metal Cations on the Electrochemical Reduction of Carbon Dioxide. *J. Am. Chem. Soc.* **2017**, *139*, 11277−11287.

(36) Hori, Y.; Takahashi, R.; Yoshinami, Y.; Murata, A. Electrochemical Reduction of CO at a Copper Electrode. *J. Phys. Chem. B* **1997**, *101*, 7075−7081.

(37) Hori, Y.; Wakebe, H.; Tsukamoto, T.; Koga, O. Adsorption of CO accompanied with simultaneous charge transfer on copper single crystal electrodes related with electrochemical reduction of CO2 to hydrocarbons. *Surf. Sci.* **1995**, *335*, 258−263 (Special issue: Proceedings of the IUVSTA Workshop on Surface Science and Electrochemistry) .

(38) Hori, Y.; Koga, O.; Watanabe, Y.; Matsuo, T. FTIR measurements of charge displacement adsorption of CO on poly- and single crystal (100) of Cu electrodes. *Electrochim. Acta* **1998**, *44*, 1389−1395.
(39) Kortlever, R.; Tan, K. H.; Kwon, Y.; Koper, M. T. M. Electrochemical carbon dioxide and bicarbonate reduction on copper in weakly alkaline media. *J. Solid State Electrochem.* **2013**, *17*, 1843−1849.
(40) Wang, L.; Nitopi, S. A.; Bertheussen, E.; Orazov, M.; Morales-Guio, C. G.; Liu, X.; Higgins, D. C.; Chan, K.; Nørskov, J. K.; Hahn, C.; Jaramillo, T. F. Electrochemical Carbon Monoxide Reduction on Polycrystalline Copper: Effects of Potential, Pressure, and pH on Selectivity toward Multicarbon and Oxygenated Products. *ACS Catal.* **2018**, *8*, 7445−7454.
(41) Dinh, C.-T.; Burdyny, T.; Kibria, M. G.; Seifitokaldani, A.; Gabardo, C. M.; García de Arquer, F. P.; Kiani, A.; Edwards, J. P.; De Luna, P.; Bushuyev, O. S.; Zou, C.; Quintero-Bermudez, R.; Pang, Y.; Sinton, D.; Sargent, E. H. CO2 electroreduction to ethylene via hydroxide-mediated copper catalysis at an abrupt interface. *Science* **2018**, *360*, 783−787.
(42) Pérez-Gallent, E.; Figueiredo, M. C.; Calle-Vallejo, F.; Koper, M. T. M. Spectroscopic Observation of a Hydrogenated CO Dimer Intermediate During CO Reduction on Cu(100) Electrodes. *Angew. Chem., Int. Ed.* **2017**, *56*, 3621−3624.
(43) Trasatti, S. The absolute electrode potential: an explanatory note (Recommendations 1986). *J. Electroanal. Chem. Interfacial Electrochem.* **1986**, *209*, 417−428.
(44) Larsen, A. H.; et al. The atomic simulation environment - a Python library for working with atoms. *J. Phys.: Condens. Matter* **2017**, *29*, 273002.
(45) Enkovaara, J.; et al. Electronic structure calculations with GPAW: a real-space implementation of the projector augmented-wave method. *J. Phys.: Condens. Matter* **2010**, *22*, 253202.
(46) Berendsen, H. J. C.; Postma, J. P. M.; van Gunsteren, W. F.; DiNola, A.; Haak, J. R. Molecular dynamics with coupling to an external bath. *J. Chem. Phys.* **1984**, *81*, 3684−3690.
(47) Hammer, B.; Hansen, L. B.; Nørskov, J. K. Improved adsorption energetics within density-functional theory using revised Perdew-Burke-Ernzerhof functionals. *Phys. Rev. B: Condens. Matter Mater. Phys.* **1999**, *59*, 7413−7421.